Atmospheric
Chemistry
and Physics

Supplement of

Measurement report: Size-resolved secondary organic aerosol formation modulated by aerosol water uptake in wintertime haze

Jing Duan et al.

Correspondence to: Ru-Jin Huang (rujin.huang@ieecas.cn)

Text S1: OA source apportionment

For OA mass spectra in each size bin during winter campaigns of 2013-2014 and 2018-2019, unconstrained PMF runs with varying factor numbers were conducted. The optimal solution for the size-resolved PMF was determined based on the principle that reducing the number of factors results in the mixing of different sources, while increasing the number of factors leads to factor splitting or mixing again and the emergence of non-meaningful factors.

Briefly, for the PMF results in each size bin in 2013-2014, the 2-factor solution resolved a POA source with prominent signal peaks at fragments such as m/z 55 (mainly $C_4H_7^+$), m/z 57 (mainly $C_4H_9^+$), and m/z 60 (mainly $C_2H_4O_2^+$), while a much lower signal at m/z 44 (mainly CO_2^+, a typical fragment in aging or secondary OA sources). These features align with typical characteristics of POA profiles reported in previous studies at various urban sites (Ng et al., 2010, 2011; Hu et al., 2016). In contrast, the second factor exhibited significantly lower signals for primary fragments like m/z 55, 57, and 60, but displayed a dominant signal peak at m/z 44, indicating its aging or secondary properties (Ng et al., 2011). Consequently, this factor was classified as a SOA source (Fig. S1). Upon increasing the factor number to 3, no distinct POA categories like HOA, COA, or BBOA were further resolved. However, the SOA factor was split into two factors, with signals at m/z 29 and m/z 44 divided in Factor 2, and signals at m/z 28 and m/z 43 divided in Factor 3, respectively (Fig. S5). Consequently, the 2-factor solution was selected as the best performance, and two OA sources, comprising POA and SOA, were identified in each size bin in 2013-2014.

For the PMF results in each size bin in 2018-2019, Factor 2 in the 2-factor solution was evidently a mixture of m/z 44 and numerous primary ions of m/z > 50, notably m/z 60 originating from BBOA (Fig. S6). This observation suggests that the 2-factor solution did not clearly distinguish between SOA and POA. Upon increasing the factor number to 3 (Fig. S3), two primary sources with much lower contribution from m/z 44, and one secondary source with dominant signal peaks at m/z 44 were resolved. Specifically, as a tracer ion for biomass burning sources, the signal of m/z 60 appeared primarily in Factor 2, with no significant mixing observed in Factor 1 and Factor 3. This indicates that Factor 2 represents a clean BBOA source identified through PMF analysis (Cubison et al., 2011). Factor 1, another primary source unaffected by m/z 60 interference, was characterized by prominent hydrocarbon ion series of C_nH_{2n-1} and C_nH_{2n+1}, defining it as a fossil-fuel-related OA (FFOA) according to previous studies (Sun et al., 2016, 2018). In comparison, Factor 3 exhibited a dominant signal peak at m/z 44, which was defined as a SOA source. The 4-factor solution was further analyzed to determine if increasing the number of factors could resolve more refined primary or secondary sources. As shown in Fig. S7, increasing the factor number to 4 resulted in newly generated factors frequently showing significant mixing, such as a mixture of BBOA and FFOA in the smaller size ranges and a blend of secondary and primary sources, especially m/z 60, in the larger size ranges. Moreover, continuing to increase the factor number to 5 did not alleviate the mixing issues, instead, other non-meaningful factors were observed (Fig. S8). Therefore, the 3-factor solution was selected as the best performance, and three OA sources, comprising FFOA, BBOA and SOA, were identified in each size bin in 2018-2019.

**Table S1** A summary of size ranges of 10 bins in the range of 80 – 2500 nm.

Bin number	Size (nm)
Bin1	80-112
Bin2	112-159
Bin3	159-225
Bin4	225-317
Bin5	317-447
Bin6	447-631
Bin7	631-890
Bin8	890-1256
Bin9	1256-1772
Bin10	1772-2500

Table S2 Evaluation of random forest regression model.

campaign	Size (nm)	RMSE[a]	R[2b]
winter 2013-2014	112-159	0.126	0.17
	159-225	0.034	0.63
	225-317	0.036	0.60
	317-447	0.049	0.73
	447-631	0.043	0.74
	631-890	0.068	0.69
	890-1256	0.052	0.67
	1256-1772	0.076	0.36
winter 2018-2019	112-159	0.196	0.09
	159-225	0.108	0.37
	225-317	0.075	0.54
	317-447	0.075	0.53
	447-631	0.066	0.61
	631-890	0.057	0.71
	890-1256	0.053	0.80
	1256-1772	0.074	0.75

[a] RMSE (Root mean square error) is the square root of the expected squared difference between the predicted and observed values.

[b]R^2 is the correlation between the observed and random forest predicted SOA%.
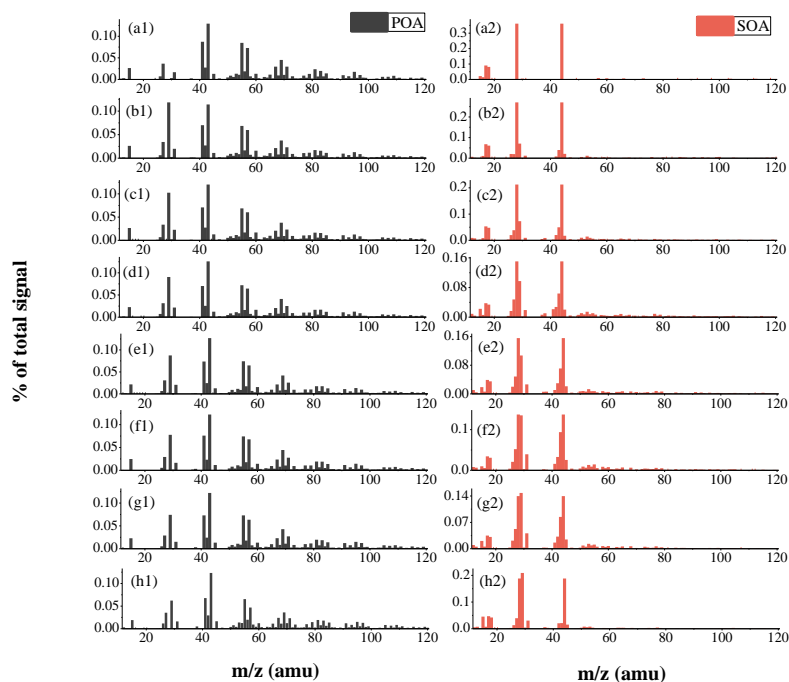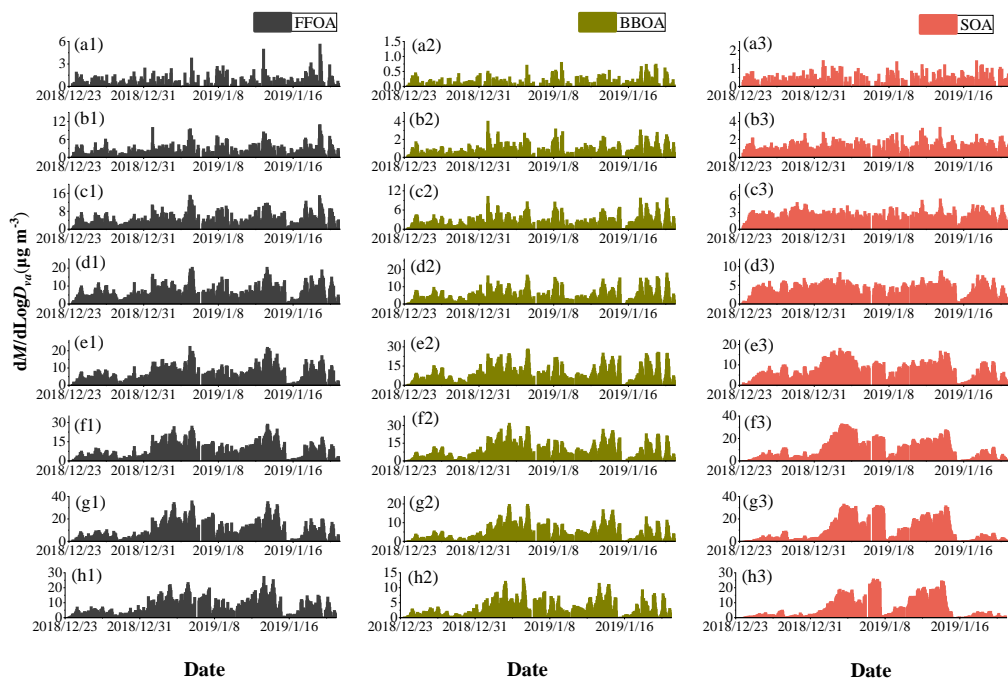
Figure S1. Mass spectra of (a1-h1) POA, (a2-h2) SOA under different size ranges of 112-159 nm, 159-225 nm, 225-317 nm, 317-447 nm, 447-631 nm, 631-890 nm, 890-1256 nm, and 1256-1772 nm, respectively, in winter 2013-2014 in Xi'an.
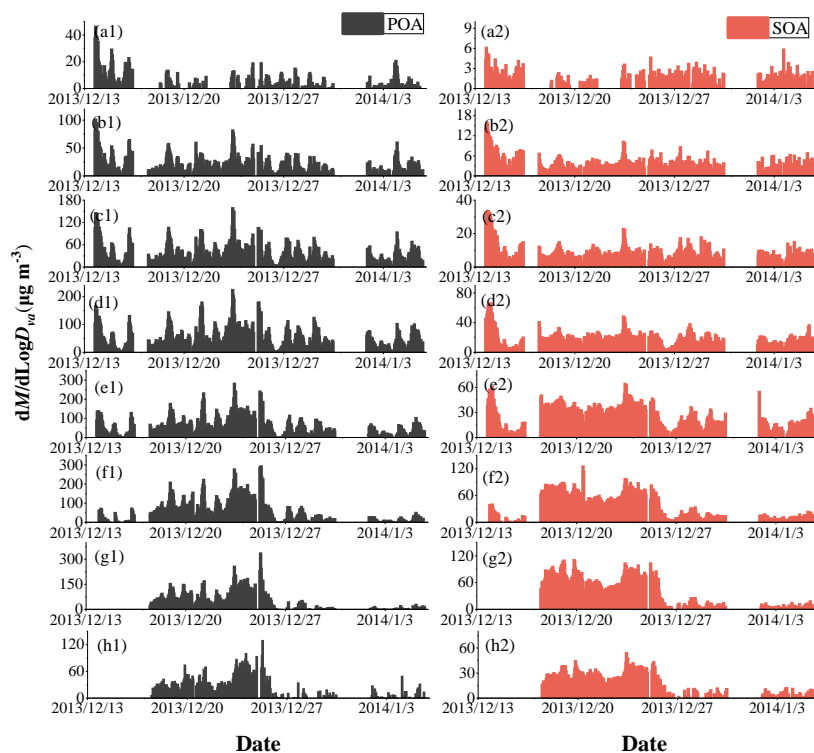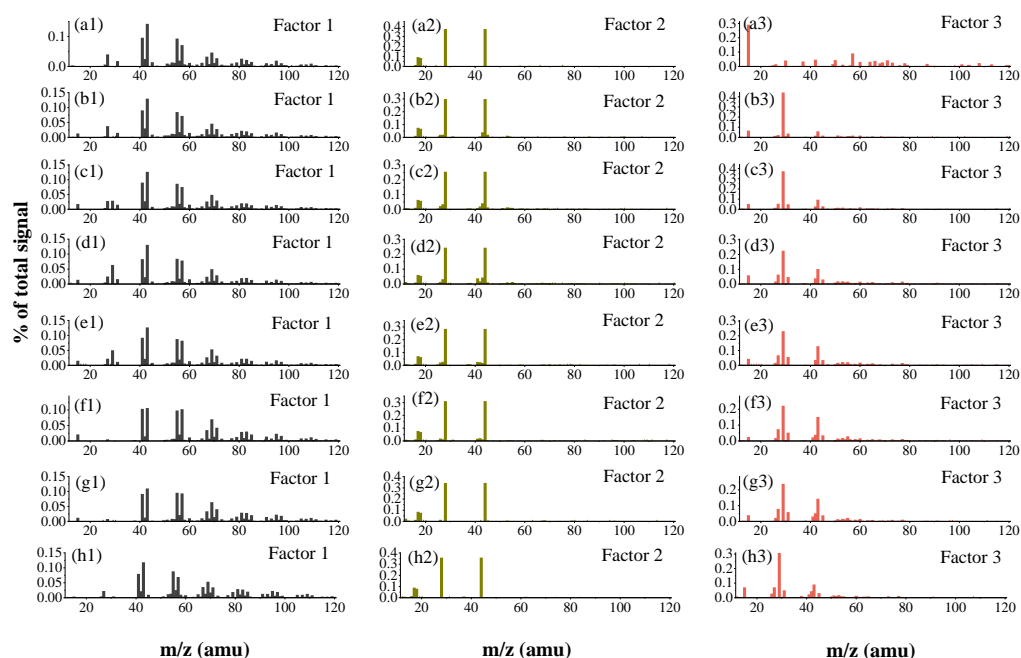

Figure S2. Time series of (a1-h1) POA, (a2-h2) SOA under different size ranges of 112-159 nm, 159-225 nm, 225-317 nm, 317-447 nm, 447-631 nm, 631-890 nm, 890-1256 nm, and 1256-1772 nm, respectively, in winter 2013-2014 in Xi'an.
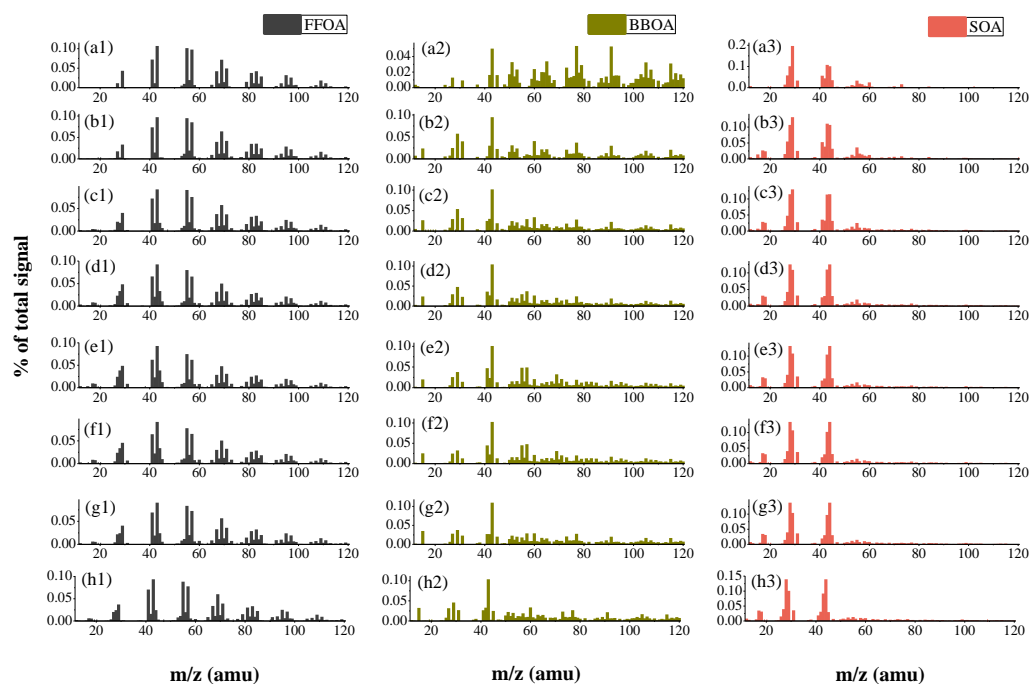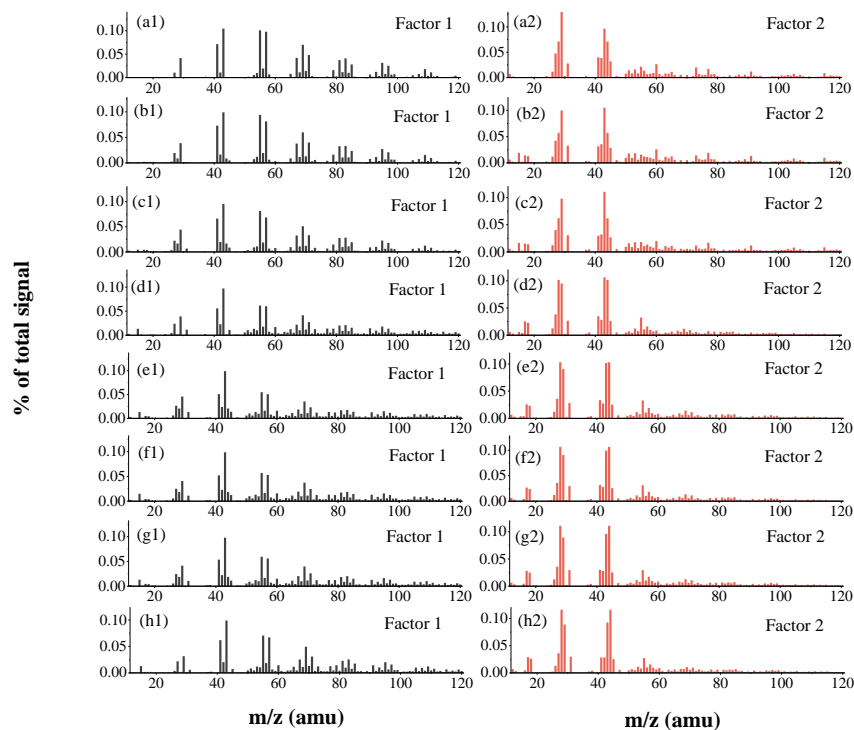
Figure S3. Mass spectra of (a1-h1) FFOA, (a2-h2) BBOA, and (a3-h3) SOA under different size ranges of 112-159 nm, 159-225 nm, 225-317 nm, 317-447 nm, 447-631 nm, 631-890 nm, 890-1256 nm, and 1256-1772 nm, respectively, in winter 2018-2019 in Xi'an.
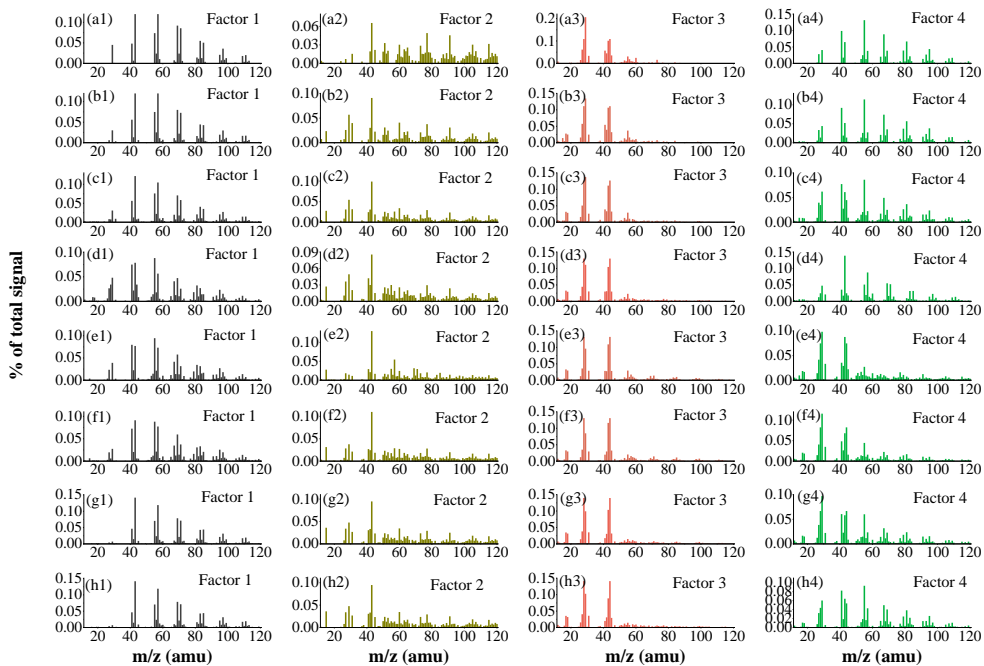

Figure S4. Time series of (a1-h1) FFOA, (a2-h2) BBOA, and (a3-h3) SOA under different size ranges of 112-159 nm, 159-225 nm, 225-317 nm, 317-447 nm, 447-631 nm, 631-890 nm, 890-1256 nm, and 1256-1772 nm, respectively, in winter 2018-2019 in Xi'an.
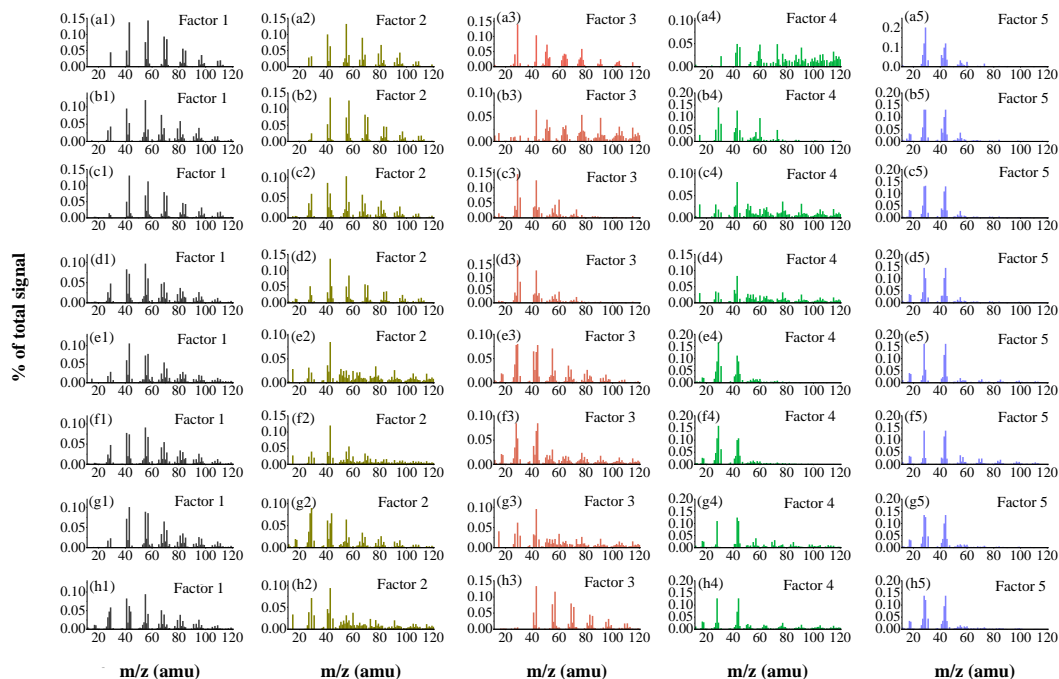
Figure S5. Mass spectra of three-factor PMF results under different size ranges of 112-159 nm, 159-225 nm, 225-317 nm, 317-447 nm, 447-631 nm, 631-890 nm, 890-1256 nm, and 1256-1772 nm, respectively, in winter 2013-2014 in Xi'an.


Figure S6. Mass spectra of two-factor PMF results under different size ranges of 112-159 nm, 159-225 nm, 225-317 nm, 317-447 nm, 447-631 nm, 631-890 nm, 890-1256 nm, and 1256-1772 nm, respectively, in winter 2018-2019 in Xi'an.

Figure S7. Mass spectra of four-factor PMF results under different size ranges of 112-159 nm, 159-225 nm, 225-317 nm, 317-447 nm, 447-631 nm, 631-890 nm, 890-1256 nm, and 1256-1772 nm, respectively, in winter 2018-2019 in Xi'an.

Figure S8. Mass spectra of five-factor PMF results under different size ranges of 112-159 nm, 159-225 nm, 225-317 nm, 317-447 nm, 447-631 nm, 631-890 nm, 890-1256 nm, and 1256-1772 nm, respectively, in winter 2018-2019 in Xi'an.
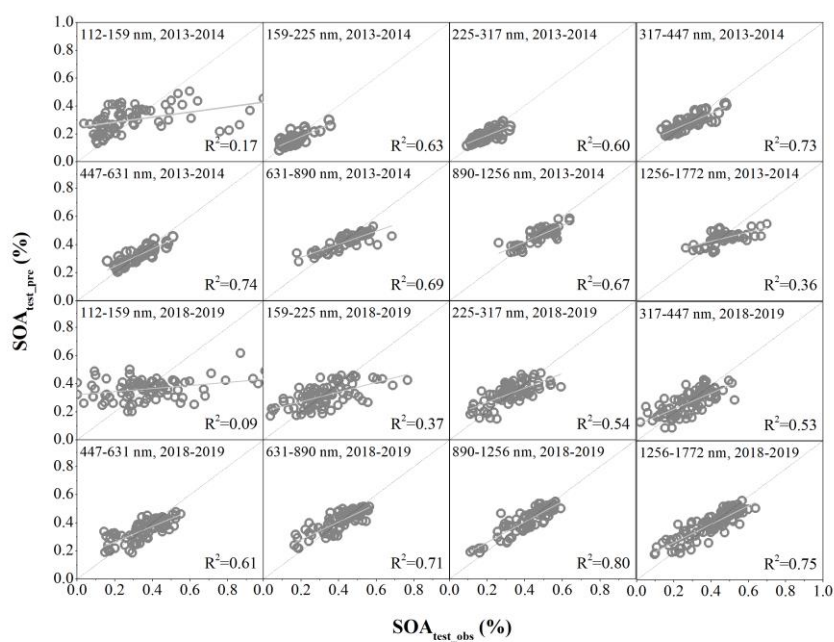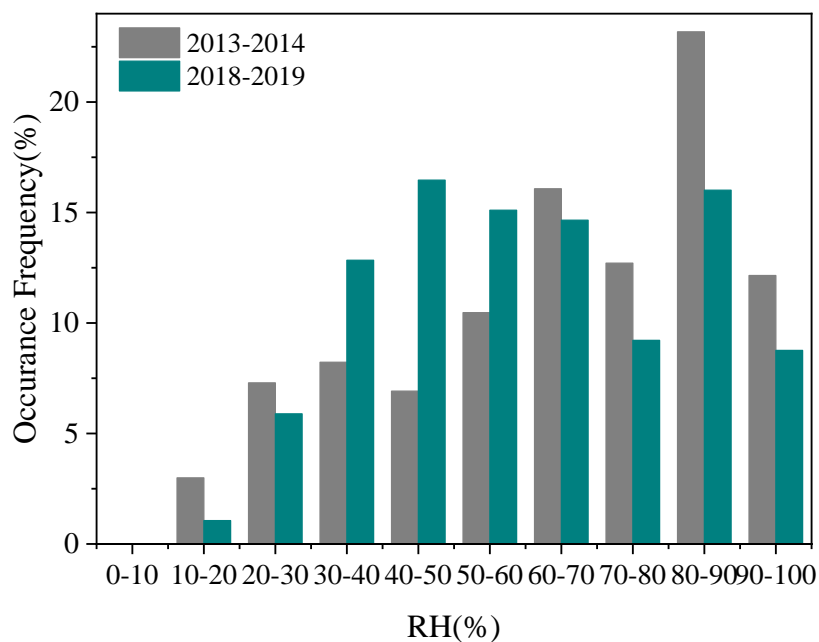
Figure S9. Correlation between the predicted and observed SOA fractions in total OA across different size ranges in the winters of 2013-2014 and 2018-2019, respectively.
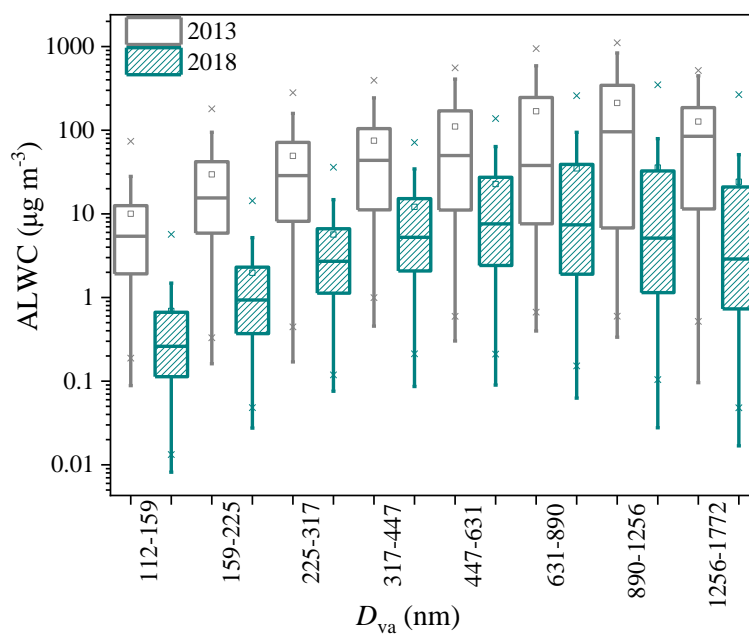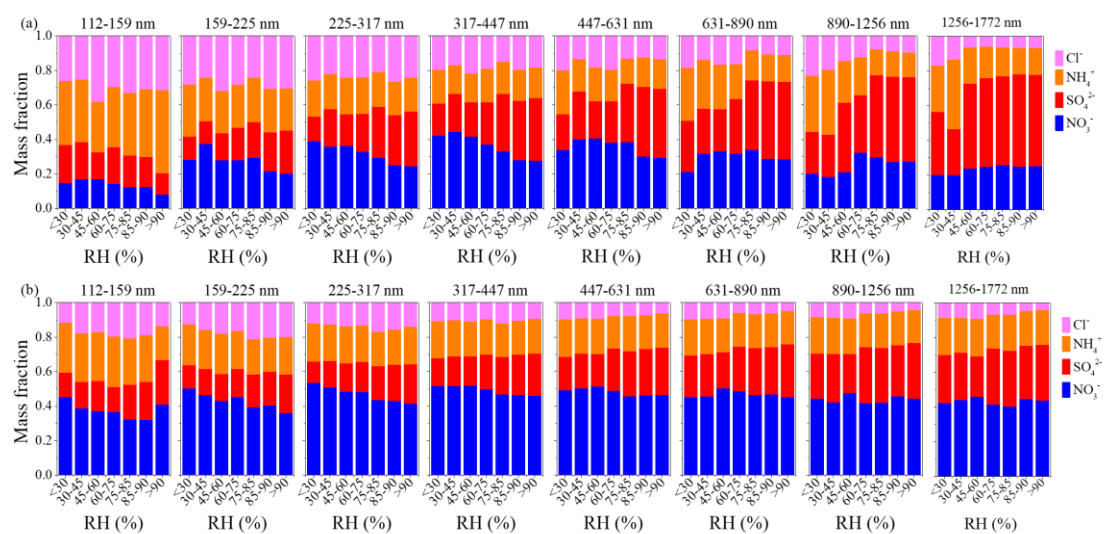

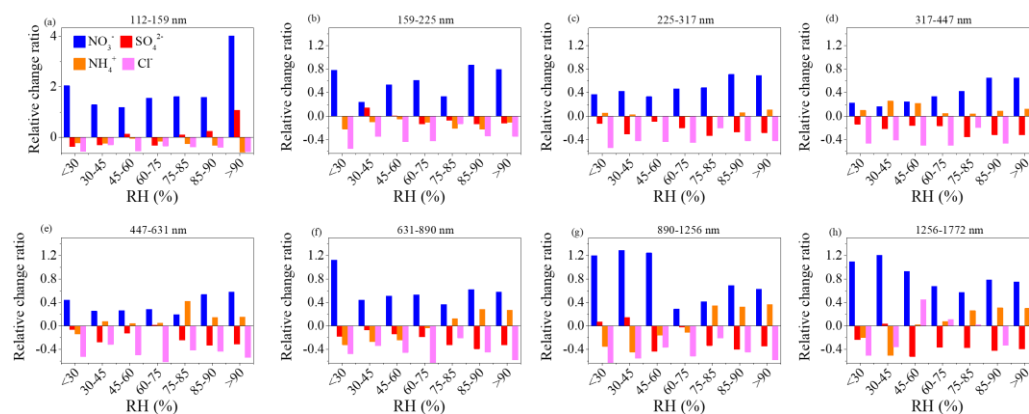**Figure S10.** Size distribution of ALWC between winter 2013-2014 and winter 2018-2019 in Xi'an.

Figure S11. Distribution frequency of RH between winter 2013-2014 and winter 2018-2019 in Xi'an.

Figure S12. Mass composition of inorganic species under different size ranges and RH ranges between winter 2013-2014 (a) and winter 2018-2019 (b).

Figure S13. Relative changes of mass fraction of NO_3^-, SO_4^{2-}, NH_4^+, and Cl^- in total inorganic aerosol in winter 2018-2019, compared to winter 2013-2014 under different size ranges.

References:

Cubison, M. J., Ortega, A. M., Hayes, P. L., Farmer, D. K., Day, D., Lechner, M. J., Brune, W. H., Apel, E., Diskin, G. S., Fisher, J. A., Fuelberg, H. E., Hecobian, A., Knapp, D. J., Mikoviny, T., Riemer, D., Sachse, G. W., Sessions, W., Weber, R. J., Weinheimer, A. J., Wisthaler, A., and Jimenez, J. L.: Effects of aging on organic aerosol from open biomass burning smoke in aircraft and laboratory studies, Atmos. Chem. Phys., 11, 12049–12064, https://doi.org/10.5194/acp-11-12049-2011, 2011.

Hu, W. W., Hu, M., Hu, W., Jimenez, J. L., Yuan, B., Chen, W., Wang, M., Wu, Y., Chen, C., Wang, Z., Peng, J., Zeng, L., and Shao, M.: Chemical composition, sources, and aging process of submicron aerosols in Beijing: Contrast between summer and winter, J. Geophys. Res.-Atmos., 121, 1955–1977, https://doi.org/10.1002/2015JD024020, 2016.

Ng, N. L., Canagaratna, M. R., Zhang, Q., Jimenez, J. L., Tian, J., Ulbrich, I. M., Kroll, J. H., Docherty, K. S., Chhabra, P. S., Bahreini, R., Murphy, S. M., Seinfeld, J. H., Hildebrandt, L., Donahue, N. M., DeCarlo, P. F., Lanz, V. A., Prévôt, A. S. H., Dinar, E., Rudich, Y., and Worsnop, D. R.: Organic aerosol components observed in Northern Hemispheric datasets from Aerosol Mass Spectrometry, Atmos. Chem. Phys., 10, 4625–4641, https://doi.org/10.5194/acp-10-4625-2010, 2010.

Ng, N. L., Canagaratna, M. R., Jimenez, J. L., Chhabra, P. S., Seinfeld, J. H., and Worsnop, D. R.: Changes in organic aerosol composition with aging inferred from aerosol mass spectra, Atmos. Chem. Phys., 11, 6465–6474, https://doi.org/10.5194/acp-11-6465-2011, 2011.

Sun, Y. L., Du, W., Fu, P., Wang, Q., Li, J., Ge, X., Zhang, Q., Zhu, C., Ren, L., Xu, W., Zhao, J., Han, T., Worsnop, D. R., and Wang, Z.: Primary and secondary aerosols in Beijing in winter: sources, variations and processes, Atmos. Chem. Phys., 16, 8309 – 8329, https://doi.org/10.5194/acp-16-8309-2016, 2016.

Sun, Y., Xu, W., Zhang, Q., Jiang, Q., Canonaco, F., Prévôt, A. S. H., Fu, P., Li, J., Jayne, J., Worsnop, D. R., and Wang, Z.: Source apportionment of organic aerosol from 2-year highly time-resolved measurements by an aerosol chemical speciation monitor in Beijing, China, Atmos. Chem. Phys., 18, 8469–8489, https://doi.org/10.5194/acp-18-8469-2018, 2018.